Materials Horizons

ROYAL SOCIETY OF CHEMISTRY

COMMUNICATION

View Article Online
View Journal

Cite this: DOI: 10.1039/d5mh00640f

Received 8th April 2025,
Accepted 21st July 2025

DOI: 10.1039/d5mh00640f

rsc.li/materials-horizons

Fine-control of electron trapping for photomultiplication in organic photodetectors by modulating the insulating properties of nonfullerene acceptors†

Min Hun Jee,‡[a] Xingchao Zhao,‡[b] Kyo Bin Park,‡[c] Min Gyu Kang,[a] Xiaoling Ma,[b] Dae Sung Chung,*[c] Fujun Zhang*[b] and Han Young Woo*[a]

Enhancing photomultiplication (PM) in organic photodetectors (OPDs) requires effective control of photogenerated trapped electrons. Conventional approaches typically adjust the conduction band of the acceptor. In this study, we present a novel strategy for precisely controlling electron trapping and trapped carrier lifetime in PM-OPDs. We synthesized a series of nonfullerene acceptors (NFAs) by modifying the ratio of conducting and insulating components in the conjugated molecular structure. By enhancing the insulating properties of the NFAs, we slowed both electron trapping and de-trapping processes. This resulted in fine-tuned trapped carrier lifetime (280–581 ms), trapped carrier density (2.04–13.4 × 10^{17} cm^{-3}), and Schottky barrier height (0.334–0.229 eV) under illumination. Higher concentrations of trapped electrons accumulated at the P3HT/Al interface, leading to a thinner Schottky barrier, reduced depletion region, and enhanced band bending, improving hole injection from the cathode. Among the NFAs, A-BTP-DT, with the highest insulating properties, exhibited superior PM effects, achieving a maximum external quantum efficiency of 7520% at −10 V (compared to 564% for the Y6-based device). This work represents the first successful demonstration of fine-tuning of electron trapping and PM effects, not by adjusting energy levels, but by modifying the insulating properties.

New concepts

This study presents a new strategy for precisely controlling electron trapping and the lifetime of trapped carriers in photomultiplication-type organic photodetectors (PM-OPDs) by tuning the insulating properties of electron acceptors. By modulating the alkyl chain length and the ratio of insulating-to-conducting regions, the insulating characteristics of the nonfullerene acceptors were successfully tailored. Enhanced insulating properties result in slower electron trapping and de-trapping dynamics, allowing for higher trapped carrier densities and prolonged lifetimes under illumination. These trapped electrons induce band bending at the active layer/cathode interface, facilitating efficient hole tunneling injection from the external circuit, which ultimately leads to enhanced photoinduced currents. This study is the first to demonstrate the effective control of electron trapping in PM-OPDs by adjusting the insulating properties around the semiconducting core, rather than the energy levels of the acceptors.

Introduction

Photodetectors convert light signals into electrical signals and are used in various applications, including image sensing, healthcare, environmental monitoring, and optical communication.[1–3] In fields such as bio-imaging and laser detection and ranging (LADAR), where detecting weak light is crucial, the sensitivity of photodetectors becomes especially important.[4–8] Enhancing sensitivity involves improving the signal-to-noise ratio, which can be achieved by increasing external quantum efficiency (EQE) or reducing dark currents.[9–14] Notably, in photomultiplication (PM)-type organic photodetectors (PM-OPDs), it is possible to achieve an EQE greater than 100%, allowing the detection of electrical signals from incident light without the need for an external amplifier.[15–19]

PM-OPDs operate as follows: the photoactive layer of a typical PM-OPD device consists of a donor polymer host with ~1% acceptor molecules dispersed within it. First, photogenerated excitons are separated at the donor–acceptor interface, creating electrons and holes. The electrons are subsequently trapped by a spatially localized acceptor, aided by its low concentration, while the holes migrate toward the collecting electrode. Second, the trapped electrons at the localized acceptor near the cathode interface cause band bending, which leads to continuous hole injection *via* tunneling effects under reverse

[a] Department of Chemistry, Korea University, Seoul 02841, Republic of Korea. E-mail: hywoo@korea.ac.kr
[b] Advanced Organic Materials and Devices Laboratory, School of Physical Science and Engineering, Beijing Jiaotong University, 100044, Beijing, People's Republic of China. E-mail: fjzhang@bjtu.edu.cn
[c] Department of Chemical Engineering, Pohang University of Science and Technology (POSTECH), Pohang 37673, Republic of Korea. E-mail: dchung@postech.ac.kr

† Electronic supplementary information (ESI) available. See DOI: https://doi.org/10.1039/d5mh00640f

‡ These authors contributed equally to this work.

bias, contributing to signal amplification. Effectively controlling electron trapping is crucial for enhancing photomultiplication. Several strategies have been suggested to achieve this, including manipulation of the lowest unoccupied molecular orbital (LUMO) energy level of acceptor materials, intramolecular traps, and interfacial electrostatic interactions.

Yoon *et al.* synthesized a series of nonfullerene acceptors (NFAs) by varying the terminal end groups (hydrogen, fluorine, chlorine, and methyl) and modulating their LUMO levels.[20] Fluorination of the NFA (ETBI-F), with the deepest LUMO level and non-isotropic molecular ordering, improved electron trapping efficiency and resulted in the longest carrier lifetime, yielding an EQE of 156 000%. Zhao *et al.* developed a strategy to reduce charge recombination by covalently linking $PC_{61}BM$ pendants to the PBDB-T polymer backbone.[21] This configuration effectively trapped photogenerated electrons within the polymer. Kim *et al.* introduced a new strategy to trap electrons by facilitating exciton scissoring—achieving exciton dissociation and immediate electron trapping without electron transport—utilizing three aryl azide-based photo-crosslinkers.[22] Furthermore, Kim *et al.* introduced the cationic conjugated polyelectrolyte PFN-Br as an electric double layer to enhance electron trapping. By controlling the counterion orientation with a protic solvent and applied bias, quaternary ammonium cations were positioned at the surface, maximizing electrostatic interaction with trapped electrons near the ITO interface. This strategy intensified Schottky interface band bending, stabilizing trapped electron states and facilitating hole injection through tunneling, thereby enhancing gain. Despite these advances, systematic approaches to fine-controlling electron trapping remain relatively underdeveloped, and much remains to be explored. The underlying physics and mechanisms of electron trapping require further investigation, particularly to understand how the molecular structure influences trapping efficiency. Further investigation in these areas requires not only improved efficiency but also greater control over charge dynamics to minimize recombination and optimize signal amplification.

In this study, we synthesized a series of NFAs—BTP-EH, BTP-HD, BTP-DT, and A-BTP-DT—with precisely modulated insulating properties by varying the alkyl chain length on the periphery and modifying the conjugated core. These modifications were aimed at controlling electron trapping and investigating the influence of the trapped carrier lifetime on the photomultiplication properties of PM-OPDs. To assess the impact of insulating properties on electron trapping, we systematically examined the correlation between the molecular structure, static and dynamic OPD device characteristics, trapped carrier concentration, trapped carrier lifetime, Schottky barrier height, and depletion region thickness. Stronger insulating properties led to longer charge lifetimes, indicating that trapped electrons remained unrecombined for extended periods, which is crucial for photomultiplication. This enhanced band bending at the Al/P3HT interface facilitated efficient hole injection from the Al electrode to the active layer *via* tunneling, ultimately improving photomultiplication performance. These findings provide valuable insights for the rational molecular design of PM-OPDs to enhance their EQE and overall performance.

Results and discussion

First, to modulate the insulating properties of NFAs, the alkyl chain length on the benzothiadiazole pyrrole (BTP) core was systematically varied, from ethylhexyl (BTP-EH or Y6) to hexyldecyl (BTP-HD) and decyltetradecyl (BTP-DT). Scheme 1 outlines the synthetic routes for the ADA-type NFAs BTP-HD and BTP-DT as well as the DA-type NFA A-BTP-DT. Detailed procedures for their synthesis are provided in the ESI.† Briefly, compound **2** was obtained with an 85.2% yield through a Stille coupling reaction of 4,7-dibromo-5,6-dinitrobenzo[*c*][1,2,5]thiadiazole and trimethyl(6-undecylthieno[3,2-*b*]thiophen-2-yl)stannane. Compound **3** or **3′** was synthesized *via* the Cadogan reaction of compound **2**, followed by alkylation with 7-(bromomethyl)pentadecane or 11-(bromomethyl)tricosane, respectively, using K_2CO_3 as a base, yielding 63% and 65%. Formylation of compound 3 was carried out *via* the Vilsmeier–Haack reaction, using excess $POCl_3$ and *N*,*N*-dimethylformamide (DMF), resulting in compound 4 with an 85% yield. Compound **4′** was obtained similarly from compound **3′** with an 85% yield. BTP-HD was then synthesized with a 58.8% yield *via* Knoevenagel condensation of compound **4** (1 equiv.) and 2-(5,6-difluoro-3-oxo-2,3-dihydro-1*H*-inden-1-ylidene)malononitrile (IC-2F, 2.5 equiv.) in the presence of pyridine, using dry chloroform (CF) as the solvent. BTP-DT was synthesized with a 67.2% yield from compound **4′**, following a procedure similar to that for BTP-HD. To further enhance the insulating properties, an asymmetric A-BTP-DT was synthesized by removing one terminal IC-2F group from BTP-DT. The Vilsmeier–Haack reaction of compound **3′** with 1 equivalent of $POCl_3$ and DMF resulted in compound **5** with an 81.1% yield. A-BTP-DT was then obtained with a 70.5% yield through Knoevenagel condensation of compound 5 (1 equiv.) and IC-2F (1.3 equiv.). The molecular structures of the intermediates, BTP-HD, BTP-DT, and A-BTP-DT, were confirmed using ^1H and ^{13}C nuclear magnetic resonance (NMR) spectroscopy and matrix-assisted laser desorption ionization-time of flight (MALDI-TOF) mass spectrometry, with all data matching the proposed structures (Fig. 1a and Fig. S11–S14, ESI†).

We conducted UV-vis absorption, cyclic voltammetry (CV), and photoluminescence (PL) measurements to investigate how variations in the alkyl chain length and the differing ratios of insulating to conducting regions affect the optical and electrochemical properties. Fig. 1b and c show the UV-vis spectra of BTP-EH, BTP-HD, BTP-DT, and A-BTP-DT in both solution and films, with Table 1 summarizing the data. In terms of alkyl chain length, the absorption maxima for BTP-EH, BTP-HD, and BTP-DT in chloroform were observed at λ_{abs} = 732, 732, and 733 nm, respectively, indicating similar absorption spectra due to their identical backbone. Regarding the ratio of insulating to conducting regions, the absorption maximum for A-BTP-DT was observed at λ_{abs} = 701 nm, showing a noticeable blue shift

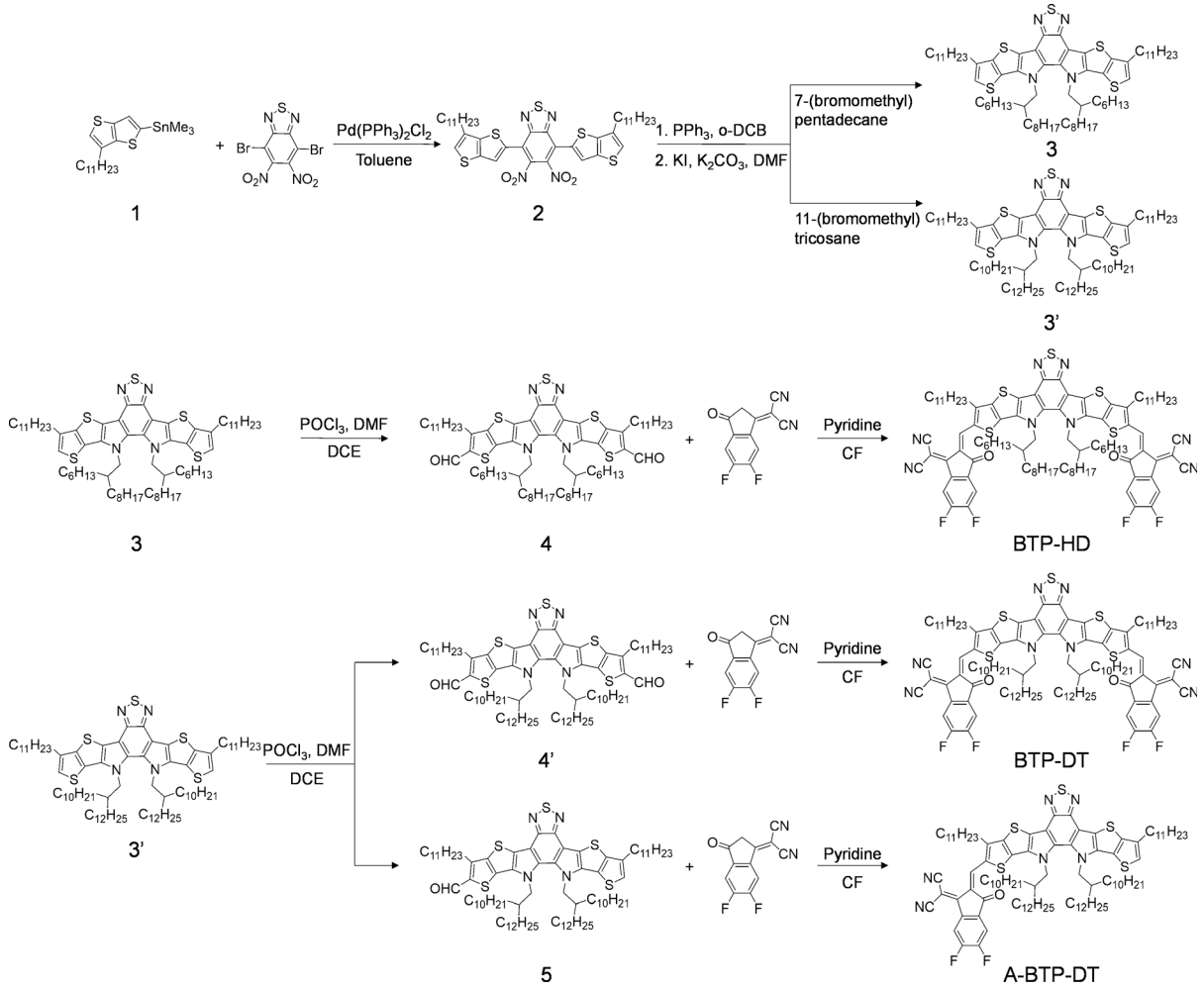

Scheme 1 Synthetic scheme of BTP-HD, BTP-DT and A-BTP-DT.

compared to BTP-DT (λ_{abs} = 733 nm). This shift can be attributed to a reduced π-conjugation length in the D–A molecular backbone of A-BTP-DT compared to the A–D–A structure of BTP-DT. In the film state, all three molecules exhibited a red shift relative to their solution spectra due to intermolecular stacking interactions. Additionally, all materials displayed complementary absorption to P3HT as the donor.

To determine the frontier molecular orbital (FMO) energy levels of P3HT, BTP-EH, BTP-HD, BTP-DT, and A-BTP-DT, cyclic voltammetry (CV) was performed, with the results shown in Fig. 1d, Table 1 and Fig. S1 (ESI†). The measurements were conducted in 0.1 M tetrabutylammonium tetrafluoroborate (Bu_4NBF_4) in acetonitrile, using $Ag/AgNO_3$ as the reference electrode, a platinum wire as the counter electrode, and a platinum electrode coated with a thin polymer donor and a small molecule acceptor film as the working electrode. A ferrocene/ferrocenium (Fc/Fc^+) couple was used as an internal standard. The highest occupied molecular orbital (HOMO) energy levels were determined from the oxidation onset potentials and were found to be −5.20, −5.70, −5.74, −5.76, and −5.57 eV for P3HT, BTP-EH, BTP-HD, BTP-DT, and A-BTP-DT, respectively. The LUMO levels were calculated based on the HOMO energy levels and the corresponding optical bandgap (E_g^{opt}), yielding −3.29 eV for P3HT, −4.39 eV for BTP-EH, −4.41 eV for BTP-HD, −4.44 eV for BTP-DT, and −4.09 eV for A-BTP-DT. The LUMO energy levels of BTP-EH, BTP-HD, and BTP-DT remain relatively unchanged despite the increasing alkyl chain lengths due to their identical conjugated backbones. However, A-BTP-DT exhibits a higher LUMO energy level and a larger bandgap compared to BTP-DT, which can be attributed to its shorter conjugation length and the absence of one electron-withdrawing IC-2F terminal group.

Next, we recorded the PL spectra of each P3HT : NFA blend film at a 100 : 4 (wt/wt) ratio under a 450 nm light source to investigate the impact of varied insulating alkyl substituents on the exciton separation yield (Fig. 1e). The PL quenching efficiencies, based on PL intensity, followed this order: P3HT:BTP-EH (98.65%) > P3HT:BTP-HD (98.15%) > P3HT:BTP-DT (97.06%) blend films. Despite the similar LUMO energy levels, we observed a gradual decrease in PL quenching efficiency in the order of BTP-EH, BTP-HD, and BTP-DT as the alkyl chain length increased. This suggests that molecules with longer

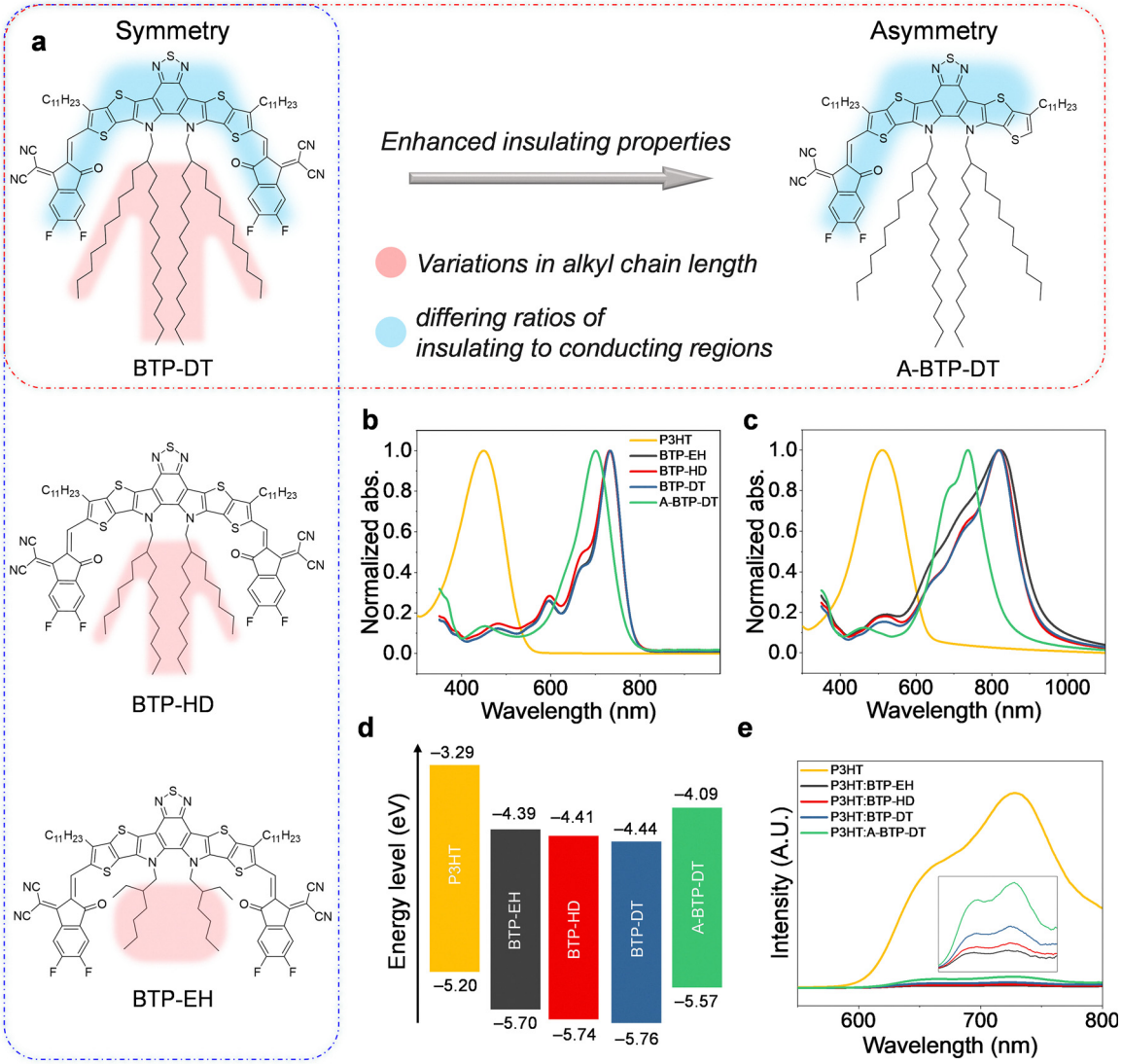

Fig. 1 (a) Molecular structures of BTP-EH, BTP-HD, BTP-DT, and A-BTP-DT. UV-vis spectra (b) in solution (CF) and (c) in films for P3HT, BTP-EH, BTP-HD, BTP-DT, and A-BTP-DT. (d) Frontier molecular orbital levels of the donor and acceptor materials. (e) Steady-state PL spectra of P3HT, P3HT:BTP-EH, P3HT:BTP-HD, P3HT:BTP-DT, and P3HT:A-BTP-DT films, with a D : A ratio of 100 : 4 (wt/wt) in the blend films.

Table 1 optical and electrochemical properties of P3HT, BTP-EH, BTP-HD, BTP-DT and A-BTP-DT

Materials	$\lambda_{abs,sol}$ [nm]	$\lambda_{abs,film}$ [nm]	$E_g^{opt\,a}$ [eV]	HOMO^b [eV]	LUMO^c [eV]
P3HT	449	511	1.91	−5.20	−3.29
BTP-EH	732	821	1.31	−5.70	−4.39
BTP-HD	732	820	1.33	−5.74	−4.41
BTP-DT	733	819	1.32	−5.76	−4.44
A-BTP-DT	701	737	1.48	−5.57	−4.09

^{a} Optical bandgaps determined from the absorption onset, $E_{opt} = \lambda_{onset}/1240$. ^{b} Determined from the onset values of oxidation potentials in CV measurements. ^{c} Calculated based on the HOMO energy levels and the corresponding optical bandgap.

insulating side chains may hinder exciton dissociation. Compared to BTP-DT, A-BTP-DT shows an even lower quenching efficiency (94.11%) due to its higher LUMO level and a larger ratio of insulating to conducting regions.

To analyze the intermolecular miscibility between the donor and acceptor, we measured the water contact angles and surface energies of thin films made from P3HT, BTP-EH, BTP-HD, BTP-DT, and A-BTP-DT (Fig. S2, ESI†). The water contact angle increases with the length of the alkyl chain in A–D–A type compounds, indicating that hydrophobicity increases in the following order: BTP-EH (94.46°), BTP-HD (96.40°), and BTP-DT (98.25°). Additionally, compared to the A–D–A type BTP-DT, the D–A type A-BTP-DT (101.21°) exhibits greater hydrophobicity due to the increased influence of the alkyl substituents surrounding the smaller conducting region. The surface energy of P3HT and the acceptors was calculated using the Girifalco–Good–Fowkes–Young equation.[23] P3HT shows a water contact angle of 99.31° and a surface energy of 15.79 mN m^{-1}.

The relatively short insulating alkyl chains in BTP-EH (19.11 mN m^{-1}) and BTP-HD (17.74 mN m^{-1}) result in a slight increase in surface energy compared to P3HT. The surface energies of BTP-DT (16.48 mN m^{-1}) and A-BTP-DT (14.58 mN m^{-1}) are closer to that of P3HT, allowing them to disperse well within the P3HT matrix, thereby maximizing the donor–acceptor interfacial area and enhancing efficient band bending in PM-OPD devices.

To further investigate the influence of NFAs with different insulating properties on the surface morphology of P3HT:NFA blend films, atomic force microscopy (AFM) measurements were performed. As shown in Fig. S3 (ESI†), the topography images of P3HT:BTP-EH, P3HT:BTP-HD, P3HT:BTP-DT, and P3HT:A-BTP-DT films exhibit smooth and uniform surfaces. The root-mean-square (RMS) roughness values were 0.636 nm, 0.819 nm, 0.743 nm, and 0.820 nm, respectively, indicating no significant morphological differences among the four blend systems.

Grazing-incidence wide-angle X-ray scattering (GIWAXS) measurements were performed on pristine P3HT, BTP-EH, BTP-HD, BTP-DT, and A-BTP-DT, as well as their corresponding blend films, to analyze the molecular orientation (Fig. S4 and S5, ESI†). In the pristine films, BTP-EH and BTP-HD exhibit a dominant face-on orientation, with the lamellar (100) peak in the in-plane (IP) direction at q_{xy} = 0.405 $Å^{-1}$ (d = 15.49 Å) and q_{xy} = 0.361 $Å^{-1}$ (d = 17.39 Å), respectively, and the prominent (010) scattering peak in the out-of-plane (OOP) direction at q_z = 1.717 $Å^{-1}$ (d = 3.66 Å) and 1.723 $Å^{-1}$ (d = 3.65 Å). While the d-spacing at the (010) peak in the OOP direction is similar for both materials, the IP (100) peak reveals that BTP-HD has a larger d-spacing than BTP-EH, which is due to the longer alkyl chains of BTP-HD. Interestingly, BTP-DT and A-BTP-DT exhibit numerous dot-like scattering peaks, suggesting their highly crystalline properties. In the blend films, due to the 100 : 4 (wt/wt) ratio of P3HT to the acceptor, the GIWAXS packing properties are dominated by P3HT, resulting in a packing pattern similar to that of P3HT (Fig. S5, ESI†).

A series of PM-OPDs were fabricated with the device structure ITO/PEDOT:PSS/P3HT:NFAs/Al. The weight ratios of P3HT to NFAs (BTP-EH) were varied (100 : 1, 100 : 4, and 100 : 7) to determine the optimal composition. Based on the J–V characteristics and photodetection properties with different weight ratios, the 100 : 4 (wt : wt) ratio was identified as the optimal condition (Fig. S6, ESI†). P3HT provides efficient hole transport channels in the active layer, leading to a high EQE of over 100% for the PM-OPDs. It is important to note that the number of trapped electrons is primarily influenced by the exciton dissociation efficiency between P3HT and NFAs, as well as the electron-capturing ability (*i.e.*, trap lifetime) of the trap materials (NFAs). The J–V curves of the PM-OPDs were first measured in the dark and under 1 mW cm^{-2} white light illumination, as shown in Fig. 2a. Here, reverse bias is defined as hole injection from the Al electrode. All four types of PM-OPDs exhibit low dark current density (J_D), resulting from the discontinuous electron channel and the large hole injection barrier from Al to the HOMO level of P3HT under dark conditions. The J_D curves of the PM-OPDs with different NFAs are nearly identical, as the hole injection barrier between Al and P3HT is similar across the devices. The light current density (J_L) is significantly larger than J_D for the PM-OPDs, benefiting from the efficient hole tunneling injection induced by trapped electrons near the Al electrode under light illumination. It is evident that the J_L of PM-OPDs increases with the extension of the insulating alkyl side chains in BTP-based NFAs. Among the devices, the PM-OPDs with A-BTP-DT show the highest J_L values, which is likely associated with the further enhanced insulating properties of asymmetric A-BTP-DT with the longest alkyl side chains. The signal-to-noise ratio (SNR) is determined by the ratio of J_{pi}/J_D (where J_{pi} is the photoinduced current density defined as the difference between J_L and J_D) at the same applied bias. As shown in Fig. 2b, the SNR as a function of voltage for four types of BTP-based NFA devices is plotted. The SNR values of the PM-OPDs increase as the insulating properties of the NFAs improve. Notably, PM-OPDs based on P3HT:A-BTP-DT exhibit the highest SNR value, reaching approximately 10^3 at −10 V, primarily due to their relatively high J_L compared to the $\sim 10^2$ observed for P3HT:BTP-EH.

The EQE spectra of the PM-OPDs were measured under a −10 V bias, as shown in Fig. 2c. The EQE values can be calculated using the following equation (1),

$$\mathrm{EQE} = \frac{J_{pi}/e}{P_{in}/h\nu} \quad (1)$$

where e is the elementary charge of the electron, h is the Planck constant, ν is the frequency of light, and P_{in} is the incident light intensity. A noticeable dip in the EQE spectra was observed from 450 nm to 550 nm for all PM-OPDs, corresponding to the strong absorption range of P3HT. Most photons in this range are absorbed by P3HT near the ITO electrode, resulting in fewer photogenerated electrons near the Al electrode. This reduction in trapped electrons near the Al electrode diminishes the efficiency of hole tunneling injection, leading to lower EQE values in this wavelength range. The PM-OPDs with A-BTP-DT as the trap material exhibit the highest EQE value (7520% at 350 nm) under a −10 V bias.

The responsivity (R = J_{pi}/P_{in}) spectra of PM-OPDs with different trap materials were measured under a −10 V bias, as shown in Fig. 2d. The PM-OPDs based on A-BTP-DT exhibit the highest R values, indicating superior photoelectric response capabilities. The maximum R is approximately 27.3 A W^{-1} at 620 nm for the PM-OPDs with A-BTP-DT. The shot noise limited detectivity (D^*_{shot}) spectra (at −10 V) with different trap materials are shown in Fig. 2e. The D^*_{shot} was determined using equation (2),

$$D^*_{shot} = \frac{R}{(2 \cdot e \cdot J_D)^{1/2}} \left(\mathrm{cm\ Hz^{\frac{1}{2}}\ W^{-1}\ or\ Jones}\right) \quad (2)$$

The PM-OPDs with A-BTP-DT exhibit excellent photodetection capabilities, with a peak D^*_{shot} of 2.7 × 10^{13} Jones at 620 nm. The measured values of J_L, EQE, R, and D^*_{shot} suggest that increasing the insulating alkyl substituents is an effective

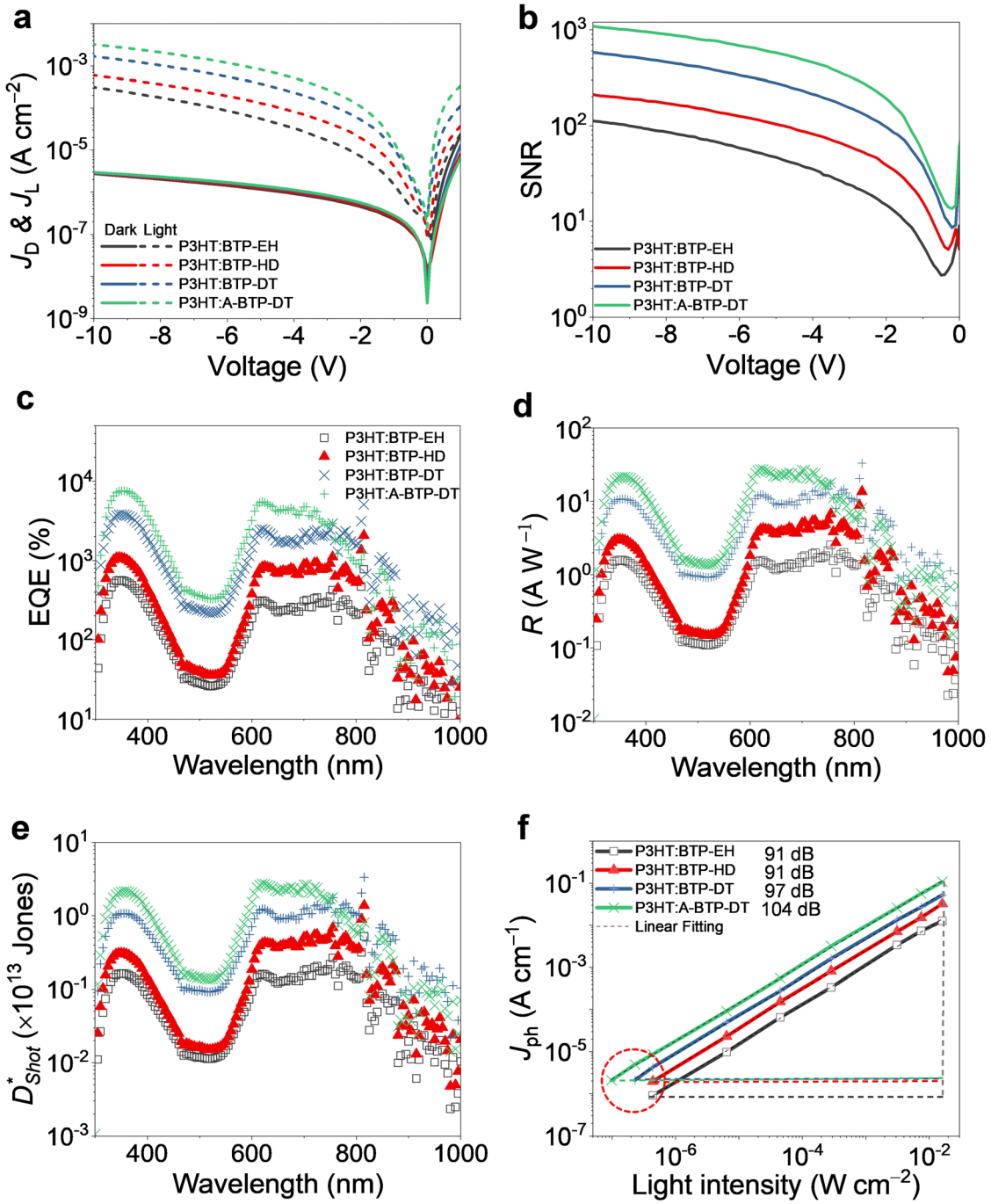

Fig. 2 PM-OPD characteristics. (a) J–V curves, (b) SNR–V curves, (c) EQE spectra, (d) responsivity spectra, (e) D^*_{shot} spectra, and (f) LDR measurements at −10 V bias for P3HT:BTP-based NFA devices.

strategy for modulating electron trapping, leading to efficient hole tunneling injection from the cathode under reverse bias. The asymmetric A-BTP-DT, with the longest alkyl side chains and smallest conjugated (or conducting) backbone, proves to be an excellent trap material for capturing electrons effectively. These results contrast with the previously discussed PL quenching data, which showed that as the alkyl chain length of the NFA increased in the P3HT:NFA blend films, the PL quenching of P3HT decreased, indicating inefficient exciton separation. The asymmetric acceptor A-BTP-DT exhibited the lowest PL quenching efficiency. The increased insulating properties of the NFA slow down the photogenerated electron transfer from P3HT to the acceptor, but simultaneously make it more difficult for trapped electrons to escape, thereby enhancing the electron trapping effect. This approach is distinctly different from previous strategies that involve controlling the LUMO level of the acceptor to increase electron trapping. It represents a simple and efficient approach to effectively fine-control electron

trapping characteristics using acceptors with similar LUMO levels, marking the first report of its kind.

To quantify the impact of modulated light power on the linear response range of OPDs, the linear dynamic range (LDR) was determined using the following equation (3),

$$\mathrm{LDR} = 20 \cdot \log\left(\frac{J_{\max}(V)}{J_{\min}(V)}\right) \quad (3)$$

where $J_{\max}(V)$ represents the maximum detectable photocurrent density and $J_{\min}(V)$ denotes the minimum detectable photocurrent density under reverse bias. As shown in Fig. 2f, the A-BTP-DT-based PM-OPD achieved a significantly higher LDR of 104 dB, compared to the BTP-EH-based OPD with the shortest alkyl substituent in trap materials (91 dB). This enhancement mainly originates from the enhanced detection of weak signals with enhanced insulating properties of NFAs (see the circle in Fig. 2f), indicating a broader and more reliable light detection range. The improved LDR is attributed to the enhanced PM effect in P3HT:A-BTP-DT, enabling the detection of weaker light signals with greater sensitivity.

To investigate the influence of trap materials on the response time of PM-OPDs, the −3 dB frequency ($f_{-3\mathrm{dB}}$) and transient photocurrent (TPC) curves were measured at a −5 V bias under 450 nm light with an intensity of 2.6×10^{-5} mW cm^{-2}, using an oscilloscope (0.5 Hz) with periodically modulated illumination. The frequency response was first determined by $f_{-3\mathrm{dB}}$, defined as the frequency at which the photoresponse decreases by −3 dB relative to the continuous wave response. The oscilloscope frequency was varied from 0.1 Hz to 10 Hz to measure the voltage and determine the resulting $f_{-3\mathrm{dB}}$ values, showing 4.32 Hz, 3.82 Hz, 2.71 Hz, and 2.08 Hz for the BTP-EH, BTP-HD, BTP-DT, and A-BTP-DT-based devices, respectively (Fig. 3a and Table S1, ESI†). The time-domain response was characterized by the rise time (τ_r) and fall time (τ_f), which represent the turn-on and turn-off times of the photodetector signals, respectively. These values are defined as the time required to reach 10–90% (τ_r) and 90–10% (τ_f) of the saturation current.[24] The τ_r/τ_f values were determined to be 80/27 ms for BTP-EH, 91/32 ms for BTP-HD, 122/37 ms for BTP-DT, and 155/43 ms for A-BTP-DT-based devices (Fig. 3b and Table S1, ESI†). Both τ_r/τ_f and $f_{-3\mathrm{dB}}$ represent the response time of the devices and they are related by the equation $\tau_r \approx 0.35/f_{-3\mathrm{dB}}$ (ESI†). Based on the calculations of τ_r and $f_{-3\mathrm{dB}}$, the response time of the devices increases in the following order: A-BTP-DT > BTP-DT > BTP-HD > BTP-EH.

The minority carrier lifetime (τ_{life}) for PM-OPDs was also determined through theoretical fitting of the transient photocurrent curves. Since the photocurrent in the PM-OPDs is generated by free holes, the transient photocurrent can be fitted with the following equation, derived from the rate equation for free hole density. This allows us to calculate the τ_{life} of the minority carrier of electrons,[20,25,26]

$$I = I_0\left(1 - \frac{1}{N_t C_2 \tau_{\mathrm{life}}}\exp\left(\frac{-t}{\tau_1}\right) - \exp\left(\frac{-t}{\tau_2}\right)\right) \quad (4)$$

where $\tau_1 = \tau_{\mathrm{life}}/(1 + N_t C_2 \tau_{\mathrm{life}})$, $\tau_2 = (1 + N_t C_2 \tau_{\mathrm{life}})/N_v' C_1$. C_2 and C_1 are constants related to the trapping and de-trapping rates, respectively. N_v' is the effective valence band density of states and N_t is the trap state density. By fitting the transient photocurrent curves to this equation, as shown in Fig. 3b, the τ_{life} values were calculated for BTP-EH, BTP-HD, BTP-DT, and A-BTP-DT devices as 280 ms, 359 ms, 478 ms, and 581 ms, respectively. This indicates that the increased insulating properties of NFAs lead to a slower de-trapping process, thereby extending the trap lifetime. This delay results in more trapped electrons near the Al electrode interface, enhancing the saturation photocurrent but also increasing the response times. Among the materials, A-BTP-DT exhibited the slowest response speed and highest saturation photocurrent due to its strongest insulating properties.

The primary role of the electron-trapping NFA in PM-OPDs is to induce band bending at the cathode/photoactive layer interface under illumination. This phenomenon is associated with the tunneling behavior of holes due to the Schottky barrier thinning effect.[27] Consequently, the Schottky junction at the Al/P3HT interface transitions into a pseudo-Ohmic junction.[20,28] This mechanism suggests that an increased number of trapped electrons at the interface accelerates the degree of band bending, thereby enhancing hole injection under illumination, which ultimately leads to higher EQE. To confirm that Schottky barrier thinning is enhanced with an increase in trapped carrier lifetime, we measured temperature-dependent *J–V* characteristics for each NFA-based PM-OPD accordingly. Assuming that the hole injection mechanism from Al to P3HT follows the thermionic emission theory,[29] which is widely accepted for Schottky junction barrier injection, the saturation current density (J_s) can be expressed as equation (5),

$$J_s = A^* T^2 \exp\left(\frac{-\phi_B}{kT}\right) \quad (5)$$

where A^* is the Richardson constant, T is the temperature, k is the Boltzmann constant, and ϕ_B is the effective Schottky barrier height. The J_s under dark conditions can be calculated using the following equation (6),[30–32]

$$J = J_s\left[\exp\left(\frac{qV}{kT}\right) - 1\right] \quad (6)$$

where q is the elementary charge and V is the applied bias voltage. To calculate the Schottky barrier height, we measured the *J–V* characteristics under various temperature conditions (220–320 K), as shown in Fig. S7 and S8 (ESI†). From these measurements, we obtained the $\ln(J_s T^{-2})$ *versus* T^{-1} plot, as shown in Fig. 3c and d. A 450 nm laser was selected as it lies outside the strongest absorption region of P3HT (around 520 nm). The effective Schottky barrier height (ϕ_B) was determined from the slope of the plot in Fig. 3c and d. The ϕ_B values under dark and illuminated conditions were found to be 0.567/0.334 eV for BTP-EH-based, 0.562/0.309 eV for BTP-HD-based, 0.545/0.258 eV for BTP-DT-based, and 0.567/0.229 eV for A-BTP-DT-based PM-OPDs (Table S2, ESI†). The effective barrier height was significantly reduced under illumination, with the

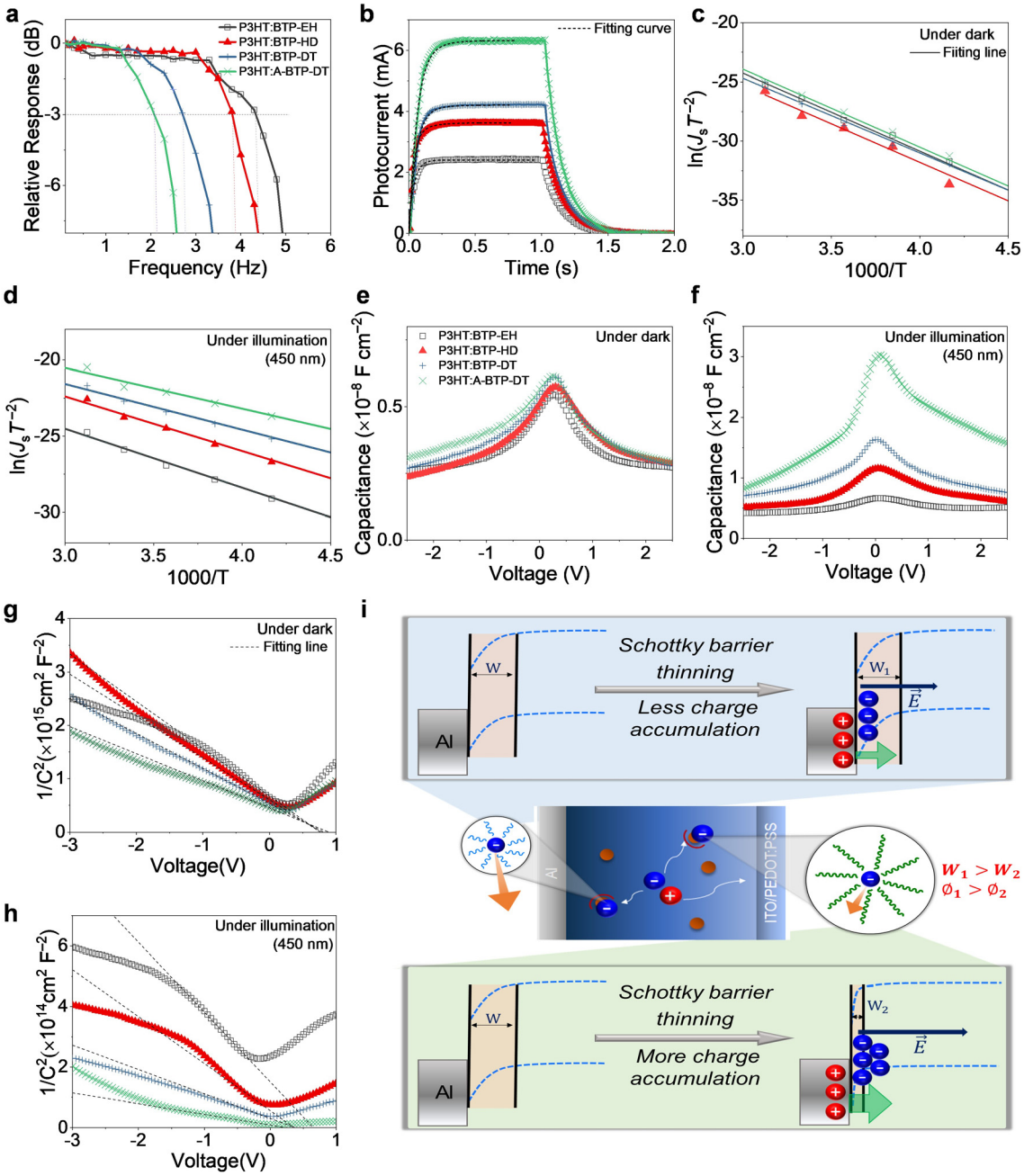

Fig. 3 (a) −3 dB cut-off frequency plots at a bias of −5 V. (b) Transient photocurrents (solid lines) and fitted transient photocurrents (dashed lines) at a bias of −5 V. $\ln(J_0 \cdot T^{-2})$ *versus* T^{-1} plots under (c) dark and (d) illuminated (450 nm) conditions for calculating the change in the effective Schottky barrier height at the cathode (Al)/photoactive layer interface. Capacitance–voltage curves under (e) dark and (f) illumination (450 nm) conditions. Mott–Schottky plots under (g) dark and (h) illuminated (450 nm) conditions. (i) Modulation of Schottky barrier thinning by controlling the insulating properties of electron trapping NFAs in PM-OPDs.

magnitude of reduction (ϕ_B under dark − ϕ_B under illumination) following the trend: A-BTP-DT (0.338 eV) > BTP-DT (0.287 eV) > BTP-HD (0.253 eV) > BTP-EH (0.233 eV). This indicates that A-BTP-DT induces the strongest band bending and, therefore, can efficiently promote hole injection through tunneling.

The Schottky barrier thinning mechanism, induced by charge accumulation at the P3HT/Al interface, is illustrated in Fig. S9 (ESI†). This mechanism is closely related to the depletion width (W) and built-in voltage (V_{bi}). We conducted light-assisted capacitance–voltage (C–V) measurements to compare the charge accumulation characteristics of each device and subsequently calculated W and V_{bi}. Since the capacitance of a device is influenced by charges at the electrode interfaces, a comparison of capacitance values allows for the estimation of trap densities. To detect trap densities from capacitance measurements, the traps are expected to influence the electrostatic potential sufficiently, forming a space charge region shorter than the semiconductor thickness.[33] In other words, when the

semiconductor layer of thickness (d) is positioned between two electrodes, the charge density is generally required to greatly exceed the surface charge density (σ) of the electrodes ($qN_q d > \sigma$), and N_q is the carrier density. To determine the pulse frequency during C–V analysis, the effects of low-frequency noise and dielectric relaxation at high frequencies were considered, and the measurements were performed at 1 kHz. Fig. 3e and f show the C–V curves of P3HT:NFA under various conditions. A comparison of the capacitance of the device under dark and 450 nm illumination conditions at zero bias revealed the following values (nF cm^{-2}): 48/66 (an increment of 18) for BTP-EH-based, 50/115 (an increment of 65) for BTP-HD-based, 53/163 (an increment of 110) for BTP-DT-based, and 55/295 (an increment of 240) for A-BTP-DT-based PM-OPDs, respectively. The trend follows: A-BTP-DT > BTP-DT > BTP-HD > BTP-EH. The increase in capacitance under illumination indicates that photogenerated electrons accumulate at the interface between the photoactive layer and the Al electrode. The difference in capacitance between dark and illuminated conditions is proportional to the amount of charge accumulated at the interface.[20] These results confirm that charge trapping increases in the order of A-BTP-DT > BTP-DT > BTP-HD > BTP-EH, demonstrating that the higher insulating properties of the NFA enable the formation of more effective traps, capable of capturing more electrons for extended periods.

At low forward and reverse biases, the capacitance of a diode follows the Mott–Schottky equation (7),[34]

$$C^{-2} = \frac{2(V_{bi} - V)}{q\varepsilon A^2 N_q} \quad (7)$$

where A is the device area, $\varepsilon = \varepsilon_0 \cdot \varepsilon_r$, ε_0 is the dielectric constant of the vacuum, and ε_r is the relative dielectric constant of the semiconductor ($\sim$3.0). Fig. 3g and h show the C^{-2}–V curves under dark and 450 nm illuminated conditions, respectively. By fitting the linear region at low bias according to the Mott–Schottky eqn (7), V_{bi} was obtained from the extrapolated intersection with the voltage axis, and N_q was calculated from the slope using the following equation (8),[34]

$$N_q = \frac{-2}{q\varepsilon_r\varepsilon_0 A^2}\left(\frac{dV}{dC^{-2}}\right) \quad (8)$$

Under 450 nm illumination, the N_q values increased significantly compared to the dark state, reflecting the trapping of photogenerated electrons at the electrode interface. Therefore, N_q can be interpreted as the trap density.[35,36] A comparison of the N_q values under dark and illuminated conditions revealed the following: $5.33 \times 10^{16}/2.04 \times 10^{17}$ cm^{-3} for BTP-EH-based, $6.00 \times 10^{16}/3.03 \times 10^{17}$ cm^{-3} for BTP-HD-based, $7.18 \times 10^{16}/5.85 \times 10^{17}$ cm^{-3} for BTP-DT-based, and $9.29 \times 10^{16}/13.4 \times 10^{17}$ cm^{-3} for A-BTP-DT-based PM-OPDs (Tables S3 and S4, ESI†). The trend of N_q increasing in the order A-BTP-DT > BTP-DT > BTP-HD > BTP-EH indicates that photogenerated electrons are most effectively trapped by A-BTP-DT. This demonstrates a correlation between the increase in the alkyl chain length and the insulating ratio of the NFA and enhanced trapping efficiency.

V_{bi} is a key factor in determining the Schottky barrier height. The reduction in the hole injection barrier upon light exposure can be derived by comparing V_{bi} under dark and illuminated conditions (Fig. 3g and h). The differences in V_{bi} between these conditions for BTP-EH, BTP-HD, BTP-DT, and A-BTP-DT-based PM-OPDs were 0.16 V, 0.43 V, 0.45 V, and 0.53 V, respectively (Tables S3 and S4, ESI†). This trend indicates that higher trapping efficiency leads to a more significant reduction in the hole injection barrier. Furthermore, electrons accumulated at the electrode/active layer interface generate a local electric field near the Al electrode. The local electric field induced by traps reduces the depletion layer width (W), as shown in Fig. S9 (ESI†), which in turn decreases the Schottky barrier height and facilitates hole tunneling injections under reverse bias. The depletion region width was calculated using the following equation (9),[34]

$$W = \sqrt{\frac{2\varepsilon(V_{bi} - V)}{qN_q}} \quad (9)$$

The calculated W values for BTP-EH, BTP-HD, BTP-DT, and A-BTP-DT-based PM-OPDs under dark conditions were 69.7 nm, 65.7 nm, 60.8 nm, and 54.1 nm, respectively. Under 450 nm illumination, the values decreased to 31.8 nm, 19.6 nm, 14.1 nm, and 8.48 nm, respectively. Since W decreases due to electron accumulation by the NFA, W follows the trend A-BTP-DT < BTP-DT < BTP-HD < BTP-EH under illuminated conditions (Table S4, ESI†). Consequently, the increase in trapped carrier lifetime due to the insulating properties leads to a higher accumulation of electrons at the interface between the electrode and the photoactive layer. This accumulation induces stronger interfacial band bending, which effectively reduces the Schottky barrier thickness and narrows the depletion region (Fig. 3i). As a result, hole injection is enhanced due to the reduced tunneling barrier, ultimately contributing to an increased saturation photocurrent and improved EQE in PM-OPDs.

Conclusions

This study explores the impact of photogenerated carrier lifetime on the photomultiplication effect in PM-OPDs. We synthesized BTP-based NFAs with varying alkyl chain lengths and insulating-to-conducting ratios to examine how insulating properties influence electron trapping. To evaluate this, we systematically explored the correlation between the molecular structure, trapped carrier lifetime and concentration, Schottky barrier height, band bending, and the resulting static and dynamic OPD characteristics. As a result, we successfully modulated the trapped carrier lifetime from 280 to 581 ms, the trapped carrier density under illumination (2.04–13.4 $\times$ 10^{17} cm^{-3}), and the effective Schottky barrier height. By enhancing the insulating properties of the NFAs, we slowed the electron de-trapping, leading to increased accumulation of trapped electrons at the P3HT/Al interface. This resulted in thinner Schottky barriers and enhanced hole injection from the cathode *via* tunneling. These findings demonstrate that tuning the insulating properties of acceptor materials effectively

controls the trapped carrier lifetime, thereby improving the PM-OPD performance.

Conflicts of interest

There are no conflicts to declare.

Data availability

The data that support the findings of this study are provided in the manuscript and the ESI.†

Acknowledgements

This work was supported by the National Research Foundation of Korea (NRF) grant funded by the Korean government (MSIT) (RS-2024-00334832 and 2023K2A9A2A06059546) and the Korea Institute for Advancement of Technology (KIAT) grant funded by the Korea government (MOTIE) (P0026257). F. Z. acknowledges the financial support from the Natural Science Foundation of Beijing (4232073) and the National Natural Science Foundation of China (Grant No. 52311540151 and U22A6002).

References

1 Q. Lin, A. Armin, P. L. Burn and P. Meredith, *Nat. Photonics*, 2015, **9**, 687–694.
2 Q. Li, Y. Guo and Y. Liu, *Chem. Mater.*, 2019, **31**, 6359–6379.
3 H. Choi, H. Kim, J. Lim, B.-J. Chang and S. Song, *Macromol. Res.*, 2024, **32**, 825–832.
4 C. X. Wang, F. Haider, X. Q. Gao, X. H. You, Y. Yang, D. F. Yuan, H. M. Aggoune, H. Haas, S. Fletcher and E. Hepsaydir, *IEEE Commun. Mag.*, 2014, **52**, 122–130.
5 Z. Zhao, C. Xu, Y. Ma, K. Yang, M. Liu, X. Zhu, Z. Zhou, L. Shen, G. Yuan and F. Zhang, *Adv. Funct. Mater.*, 2022, **32**, 2203606.
6 T. Yan, Z. Li, F. Cao, J. Chen, L. Wu and X. Fang, *Adv. Mater.*, 2022, **34**, 2201303.
7 Z. Zhao, Z. Hu, M. Deng, E. Hong, P. Wang, Z. Li and X. Fang, *Adv. Mater.*, 2025, **37**, 2416033.
8 Y. Hu, X. Zhang, X. Mo, J. Chu, X. Fang and Z. Li, *Adv. Funct. Mater.*, 2025, **35**, 2412015.
9 M. H. Jee, B. Park, A. Y. Lee, S. Rhee, M. Lim, J. M. Ha, N. Kim, F. Zhang, J.-W. Ha, H. Ahn, J. H. Kim, M. Han, S. C. Yoon, S.-J. Ko and H. Y. Woo, *Chem. Eng. J.*, 2024, **490**, 151624.
10 H. Zhang, X. Zhao, R. Gong, K. Yang, N. Kim, X. Ma, L. Lu, H. Y. Woo and F. Zhang, *ACS Appl. Electron. Mater.*, 2024, **6**, 8481–8487.
11 H. M. Luong, S. Chae, A. Yi, J. Chatsirisupachai, B. M. Kim, Y. Wan, V. Promarak, H. J. Kim and T.-Q. Nguyen, *Matter*, 2024, **7**, 2473–2489.
12 K. Kranthiraja, H. Kim, J. Lee, U. K. Aryal, S. S. Reddy, R. D. Gayathri, T. Gokulnath and S.-H. Jin, *Macromol. Res.*, 2023, **31**, 897–905.
13 K. Yang, X. Zhao, B. Wang, X. Ma, L. Lu, J. Wang, G. Xing and F. Zhang, *Adv. Funct. Mater.*, 2025, **35**, 2415978.
14 M. Lim, X. Ma, Y. Kang, M. H. Jee, S. Lee, S. Y. Jeong, T. H. Kim, J. W. Shim, F. Zhang and H. Y. Woo, *Chem. Eng. J.*, 2025, **504**, 158769.
15 X. Zhao, M. Liu, J. Wang, K. Yang, H. Zhang, S. Y. Jeong, X. Ma, H. Y. Woo and F. Zhang, *ACS Appl. Mater. Interfaces*, 2024, **16**(27), 35400–35409.
16 M. I. Kim, S. Lee, J. Kang, J. Kim, Z. Wu, J. H. Won, S. Baek, D. S. Chung, J. Y. Kim, I. H. Jung and H. Y. Woo, *Adv. Mater.*, 2024, **36**, 2404597.
17 S. Li, Y. Wang, L. Hao, Z. Tan, Y. Huang, W. Zhong, S. Dong, X. Yang and F. Huang, *Adv. Funct. Mater.*, 2025, **35**, 2415142.
18 M. Jeong, S. G. Han, W. Sung, S. Kim, J. Min, M. K. Kim, W. Choi, H. Lee, D. Lee, M. Kim and K. Cho, *Adv. Funct. Mater.*, 2023, **33**, 2300695.
19 J. Huang, J. Lee, M. Schrock, A. L. Dixon, A. T. Lill, K. Cho, G. C. Bazan and T.-Q. Nguyen, *Mater. Horiz.*, 2020, **7**, 3234–3241.
20 S. Yoon, G. S. Lee, K. M. Sim, M.-J. Kim, Y.-H. Kim and D. S. Chung, *Adv. Funct. Mater.*, 2021, **31**, 2006448.
21 Z. Zhao, B. Liu, C. Xu, L. Li, M. Liu, K. Yang, S. Y. Jeong, H. Y. Woo, G. Yuan, W. Li and F. Zhang, *J. Mater. Chem. C*, 2022, **10**, 7822–7830.
22 J. Kim, H. Kweon, M. Lee, M. Kang, S. Lee, S. An, W. Lee, S. Choi, H. Choi, Y. Seong, H. Ham, H. Cha, J. Lim, D. H. Kim, B. Kim and D. S. Chung, *Adv. Mater.*, 2023, **35**, 2302786.
23 K. Grundke, Surface-energetic properties of polymers in controlled architecture, *Molecular Interfacial Phenomena of Polymers and Biopolymers*, ed. P. Chen, Woodhead Publishing, Cambridge, 2005, ch. 10, pp. 323–374.
24 J. Miao and F. Zhang, *Laser Photon. Rev.*, 2019, **13**, 1800204.
25 J. Kim, M. Kang, S. Lee, C. So and D. S. Chung, *Adv. Mater.*, 2021, **33**, 2104689.
26 T. Park, S. Lee, M. Kang, S. H. Yu, G.-H. Nam, K. M. Sim and D. S. Chung, *Chem. Eng. J.*, 2021, **418**, 129354.
27 M. Kang, A. K. Harit, H. Y. Woo and D. S. Chung, *J. Mater. Chem. C*, 2022, **10**, 15160–15167.
28 D. K. Neethipathi, H. S. Ryu, M. S. Jang, S. Yoon, K. M. Sim, H. Y. Woo and D. S. Chung, *ACS Appl. Mater. Interfaces*, 2019, **11**, 21211–21217.
29 S. M. Sze, *Semiconductor Devices: Physics and Technology*, Wiley, New York, 2nd edn, 2002.
30 J. Osvald and Z. J. Horváth, *Appl. Surf. Sci.*, 2004, **234**, 349–354.
31 S. Lee, G. S. Lee, M. Kang, Y. H. Ha, Y.-H. Kim and D. S. Chung, *Adv. Funct. Mater.*, 2022, **32**, 2204383.
32 X. Ma, H. Bin, B. T. van Gorkom, T. P. A. van der Pol, M. J. Dyson, C. H. L. Weijtens, M. Fattori, S. C. J. Meskers, A. J. J. M. van Breemen, D. Tordera, R. A. J. Janssen and G. H. Gelinck, *Adv. Mater.*, 2023, **35**, 2209598.
33 J. Siekmann, S. Ravishankar and T. Kirchartz, *ACS Energy Lett.*, 2021, **6**, 3244–3251.
34 T. Kirchartz, W. Gong, S. A. Hawks, T. Agostinelli, R. C. I. MacKenzie, Y. Yang and J. Nelson, *J. Phys. Chem. C*, 2012, **116**, 7672–7680.
35 W. Gong, T. An, X. Liu and G. Lu, *Chin. Phys. B*, 2019, **28**, 038501.
36 Y. Song, Z. Zhong, P. He, G. Yu, Q. Xue, L. Lan and F. Huang, *Adv. Mater.*, 2022, **34**, 2201827.

